International Journal of Solids and Structures 190 (2020) 119–128

Contents lists available at ScienceDirect

International Journal of Solids and Structures

journal homepage: www.elsevier.com/locate/ijsolstr

Mechanical behavior of cellular networks of fiber bundles stabilized by adhesion

V. Negi, R.C. Picu*

Department of Mechanical, Aerospace and Nuclear Engineering, Rensselaer Polytechnic Institute, Troy, NY 12180, United States

ARTICLE INFO

Article history:
Received 17 September 2019
Revised 23 October 2019
Accepted 4 November 2019
Available online 5 November 2019

Keywords:
Fiber networks
Mechanical behavior
Adhesion
Hyperelastic

ABSTRACT

In this work, we study the mechanical behavior of non-crosslinked networks of fibers that interact adhesively. Adhesion drives fiber organization into bundles and a network of fiber bundles forms as a result of this process. Bundles split and re-connect forming specific triangular features at all bundle intersections, with role in network stabilization. The structure of such networks has been discussed in the literature, but their mechanics remains largely unexplored. We show here that such networks are exceptionally stable, and despite the absence of crosslinks between fibers behave, at relatively small strains, essentially similar to crosslinked networks, in which the role of crosslinks is played by the triangular structures at bundle intersections. We also provide new results regarding the effect of the network architecture on the type of strain stiffening observed in tension. The results apply to carbon nanotube structures, such as buckypaper, and various connective biological tissue in which collagen fibrils form bundles and the tissue is a network of collagen fibril bundles.

1. Introduction

Many biological and man-made soft materials have a network of fibers as their main structural component. The extra-cellular matrix (ECM) and connective tissues in animals are composed from collagen and elastin fibers. F-actin networks and microtubules are structural components of the cytoskeleton in eukaryotic cells. Networks of polymeric nanofibers, like polyacrylonitrile (PAN), poly-L-lactide (PLLA), polypropylene (PP) etc., are used in applications like textile, filtration, hygiene products, and tissue engineering. The prevalence of fibrous materials in the biological world is due to the effectiveness of reinforcement provided by fibers: small volumes of material are used to span large spatial domains and provide adequate stiffness and strength. Soft materials composed from molecular networks such as rubber, gels and some adhesives accommodate large deformations and generally exhibit high toughness (Ducrot et al., 2014; Gong, 2014).

In random fibrous assemblies, fibers interact at points of contact where they may be rigidly bonded to each other (crosslinks), or not. In the absence of crosslinks, topological interactions, associated with the fiber non-overlapping condition, become the controlling factor in the mechanics of the fibrous assembly (Schofield, 1938; Subramanian and Picu, 2011; Toll and Manson, 1995; van Wyk, 1946). This is the situation in clumps of fibers such as wool and insulation material subjected to compression.

Surface interactions between fibers are often of adhesive type. Adhesive interactions originate from various sources such as hydrophobic attraction between filaments, hydrogen bonding, electrostatic interactions, etc., each being dominant in specific material system. Adhesion forces are generally short-ranged, and in order to engage the interaction, fibers must be brought in contact in some other way. For example, non-wovens are 'mechanically activated' in order to increase their stiffness and strength (Michielsen et al., 2006), wet pulp is compressed to bring the cellulose fibers in contact in order to form paper (Alava and Niskanen, 2006), while capillarity may organize wet fibrous assemblies into bundles (Bico et al., 2004; De Volder and Hart, 2013) as reviewed in Style et al. (2017). In such cases, capillary forces bring the elastic fibers in contact, after which they are held together by adhesive forces.

At the scale of a pair of fibers interacting adhesively one may envision two types of configurations: a crossed configuration, in which fibers meet at a non-zero angle and the contact is established over an elliptical domain of size of the order of the fiber diameter, and a parallel configuration, in which fibers are in contact all along their length. The first scenario is encountered mostly in mats of spun fibers (Negi and Picu, 2019a), while the second is observed in networks of fibers that self-organize under the action of adhesion (Sengab and Picu, 2018). In the second case, fibers form

* Corresponding author.
E-mail address: picuc@rpi.edu (R.C. Picu).

https://doi.org/10.1016/j.ijsolstr.2019.11.003
0020-7683/

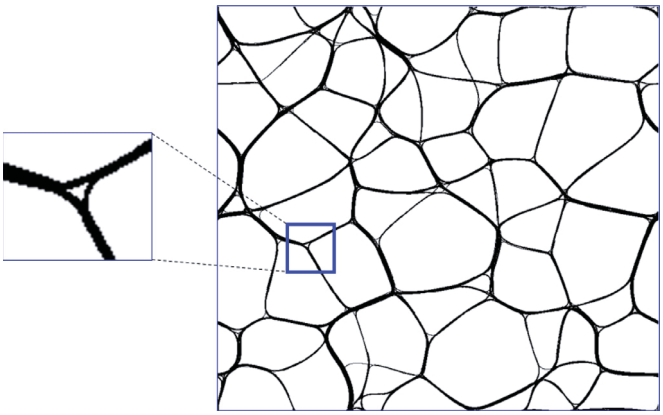

Fig. 1. Cellular network of fiber bundles stabilized by adhesion obtained using a bead-spring model evolved with molecular dynamics in Picu and Sengab (2018). The inset shows the triangular structure of a node of the network.

bundles which are held together by adhesive forces. The formation of filament bundles was observed in dense suspensions of actin (Tempel et al., 1996) and collagen (Yunoki et al., 2015) and the process was discussed theoretically by Zilman and Safran (2003).

An analysis of the structural organization driven by adhesive forces in non-bonded fiber assemblies was presented in Picu and Sengab (2018). In this work, fibrous systems were represented with the bead-spring model commonly employed in polymer physics and were allowed to evolve under the action of adhesive forces. The organization and stability of the resulting structure was analyzed. Fibers tend to bundle, and a random network of bundles results gradually. Fig. 1 shows such an example. The nodes of this network have a special structure. Nodes are generally three-fold coordinated (connectivity number $z=3$), i.e. represent the intersection of three bundles. At given node, each bundle splits and the resulting sub-bundles merge with the other bundles involved, as shown in the inset of Fig. 1. This triangular structure is similar to the Plateau triangles observed in foams, plays a central role in network stabilization, and was first described and analyzed in detail in Picu and Sengab (2018).

The evolution of an assembly of fibers under the action of adhesive forces is controlled by two non-dimensional groups: ρL_0, where L_0 is the fiber length, while ρ is the network density (total length of fibers per unit projected area of the network), and $\Psi=(L_0/L_{EC})^2$, where $L_{EC}=\sqrt{E_f I_f/\gamma}$ is the elastocapillarity length (Bico et al., 2004). E_f and I_f are the elastic modulus of the fiber material and the moment of inertia of the fiber cross-section, while γ represents the work of adhesion per unit length of contact between two fibers with parallel axes. For 'infinite' fibers, i.e. fibers which are much longer than the pore size or any other microstructural length scale, Ψ can be defined in terms of the fiber diameter, d_f, which is the only intrinsic length scale of the problem. In the present case, we work with $\Psi_d=(d_f/L_{EC})^2$.

It was shown in Picu and Sengab (2018) that fibrous systems evolve when $\Psi > a(\rho L_0)^2$, where a is a numerical constant, and remain in the as-deposited ('locked') state when this condition is not fulfilled. Large Ψ values result if adhesion is strong (γ is large) or when $E_f I_f$ is small. Since $I_f \sim d_f^4$, both Ψ and Ψ_d increase rapidly as d_f decreases, and hence networks of nanofibers are much more likely to self-organize under the action of adhesion compared with networks of microfibers. Further, if ρL_0 is small, evolving structures may disintegrate into isolated bundles, while a cellular network of fiber bundles forms at larger ρL_0. Inter-fiber friction leads to an increase of constant a and renders self-organization and structural evolution less likely (Sengab and Picu, 2018). The results reported in Sengab and Picu (2018) allow determining whether a specific system is expected to evolve under the action of adhesion such to form a network of bundles or not. These two articles, Picu and Sengab (2018) and Sengab and Picu (2018), introduce cellular networks and identify the parametric regime in which such networks exist in the presence and in the absence of inter-fiber friction, but do not discuss the mechanics of the resulting fibrous structures. The analysis of the mechanical behavior of cellular networks is the objective of the present article. The mechanics of 'locked' fiber mats in which non-crosslinked fibers interact by adhesion and friction, but the network is not of self-organized, cellular type is presented in Negi and Picu (2019a).

Buckypaper is an example of a network of bundles (Berhan et al., 2004; Coleman et al., 2003; Liu et al., 1998; Lu, 1997). L_{EC} is very small (L_{EC} = 10 nm) for single-walled CNT (10,10) of diameter 1.4 nm, which leads to large Ψ values even for relatively short CNTs (small L_0). This can be compared for example, with PAN nanofibers of diameter 300 nm, for which $L_{EC} \sim 30\,\mu$m and which are less likely to self-organize in networks of bundles under the action of surface interactions. Fibers with diameter larger than 1 μm are even less likely to self-organize.

Consider now the expected behavior of such networks when subjected to tensile loading. Two distinct classes of response exist function of whether fibers can slide relative to each other within bundles or not. If fibers are allowed to slide axially, bundles behave similar to elastic-plastic rods in tension, may thin down and rupture. The effective yield stress depends on the magnitude of friction. At the nanoscale, friction is not Coulombic and is characterized by a constant shear stress, independent of the load acting normal to the contact surface (Carpick et al., 1996; Homola et al., 1990). Hence, the force required to pull two parallel fibers in adhesive contact is proportional to the length of the contact between fibers. This renders sliding along the contour of fibers within bundles unlikely in realistic situation. In buckypaper, which is the prototypical example of cellular networks stabilized by adhesion, the network ruptures before extensive sliding occurs (Stallard et al., 2018). If relative sliding is not pronounced, bundles deform elastically, and nodal triangles evolve leading to dynamic splitting and merging of sub-bundles. We focus the present study on this deformation regime of cellular networks and seek to quantify the role of the adhesive interactions and network elasticity in defining the mechanics of the network.

2. Model and simulation procedure

2.1. Network geometry parametrization

The networks considered in this study are similar to that shown in Fig. 1, i.e. they are planar, and the nodes have connectivity $z=3$. We assume that all bundles contain the same number of fibers, n. In realistic structures, n may fluctuate to some extent between bundles forming the network, but this detail is neglected here for simplicity. Symmetry considerations mandate that, under these conditions, bundles meet at 120° if the node is isolated from the network. The inter-bundle angles deviate from 120° if the values of n of the three bundles forming a given node are not equal. However, for a broad distribution of n values, the inter-bundle angles deviate only slightly from the perfectly symmetric configuration (Appendix A), observation which supports the modeling choice made here.

Two cases are considered (Fig. 2): Case (1) represents the nominal cellular network situation, in which nodal triangles are present at all network nodes, while Case (2) is a limit situation in which the nodal triangles collapse to a point, which becomes a network node. The underlying graph topology is assumed to be of Voronoi type. Rens et al. (2016) considered a 2D network of connectivity

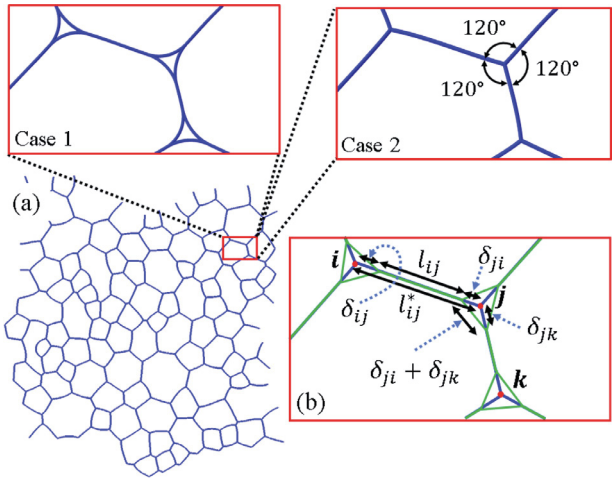

Fig. 2. (a) Realization of a cellular network showing the two cases discussed in text. Case (1) represents nominal cellular networks with nodal triangles, whereas Case (2) represents the corresponding structure without nodal triangles, but same graph. The geometric parameters used in the analysis in Case (1), $\{l^*_{ij},\ \delta_{ij}, \delta_{ji}\}$, are shown in (b).

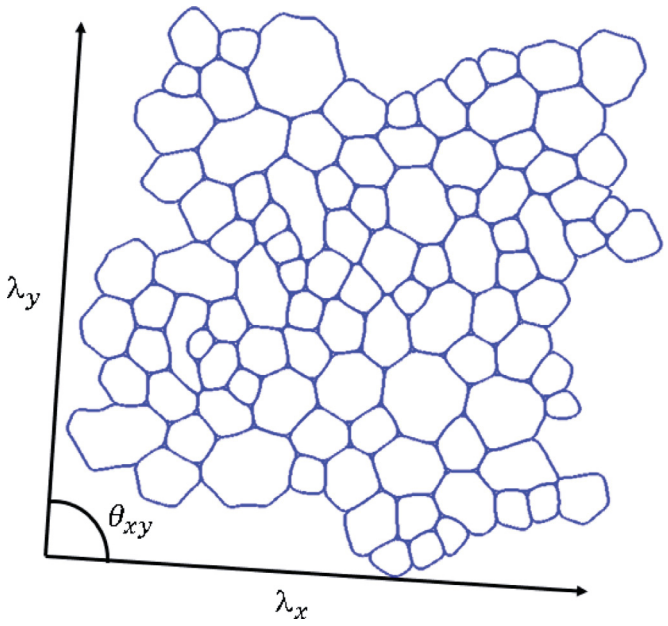

Fig. 3. Periodic nominal cellular network structure, $\mathcal{S}$.

equal to, or smaller than 3 at all nodes and stabilized by bending interactions, somewhat similar to Case (2) considered here.

The geometry is parametrized by the bundle length l_{ij} corresponding to the generic link between nodes i and j of the network, and by nodal triangle parameters $\delta_{il}, \delta_{im}, \delta_{in}$ where l, m, n are the three nodes connected to node i (Fig. 2(b)). With l^*_{ij} being the maximum length of link ij, it results that $l_{ij} = l^*_{ij} - \delta_{ij} - \delta_{ji}$. The average of l_{ij} over the entire structure is denoted by l_C, $l_C = \overline{l_{ij}}$. Case (2) is equivalent to Case (1) in the limit $L_{EC} \ll l_C$. The set $\{l^*_{ij},\ \delta_{ij}, \delta_{ji}\}$, along with the graph topology, defines the parametric model, denoted by $\mathcal{M}$. For a given $\mathcal{M}$, the corresponding network structure, denoted by $\mathcal{S}$, is obtained through a finite element (FE) simulation.

2.2. Model generation

The procedure starts with the generation of a Voronoi network which is then used as the underlying graph for the geometric parametrization to obtain $\mathcal{M}$. For any given $\mathcal{M}$, the bundles are represented using 2D linear Timoshenko beam elements with circular cross-section and with at least 5 elements per bundle. Multi-Point Constraints (MPC) are also used to connect the mesh representing the bundles with the sub-mesh representing the nodal triangles. This produces bundle branches in the nominal cellular network structure, $\mathcal{S}$.

The moment of inertia of the bundle section is denoted by I_b. A bundle comprising n constituent fibers which may slide axially relative to each other has $I_b = nI_f$. If no fiber sliding takes place, the bundle section is rigid and $I_b \sim n^2 I_f$ in the large n limit. In this work we consider the low friction and/or relatively low n case, such that $I_b = nI_f$. The equivalent diameter of a bundle results $d_b = n^{1/4} d_f$.

FE simulations to obtain the actual structure $\mathcal{S}$ (Fig. 3) from a given parametric model $\mathcal{M}$ are performed using the commercial finite element package ABAQUS-v11. The explicit time integration scheme is used with appropriate time-stepping to ensure numerical convergence.

Further, while preserving the graph structure (general connectivity) of the initial Voronoi network and the network density, the total energy, U_T, of the network structure, $\mathcal{S}$, is minimized in the phase space defined by parameters $\{l_{ij}, \delta_{ij}\}$. Note, $U_T = U_S + U_\gamma$ where U_S is total strain energy and U_γ is the total adhesion energy. The energy minimization procedure involves the network structure, $\mathcal{S}$, evolution under the combined action of two processes – process-A and process-B – corresponding to the variation of U_T with l_{ij} and δ_{ij}, respectively.

Process-A changes the bundle lengths (outside of nodal triangles), while keeping the length of the nodal triangle sub-bundles constant. It is driven by the gradient of U_T (or U_S) in the phase space of $\{l_{ij}\}$, which is calculated using a semi-analytical expression. For a bundle of length l_{ij}, bending energy u_{BE}, axial energy u_{BE}, and shear energy u_{SE} (Fig. 4(a)), $\partial U_T/\partial l_{ij}$ is obtained as (see Appendix B):

$$\frac{\partial U_T}{\partial l_{ij}} = \frac{\partial U_S}{\partial l_{ij}} = -\frac{(u_{BE} + 3u_{AE} + 3u_{SE} + \boldsymbol{r}_{12}\cdot\boldsymbol{F}_2)}{l_{ij}} \tag{1}$$

where, $\boldsymbol{r}_{12}$ is the position vector of bundle end 2 relative to the bundle end 1, and $\boldsymbol{F}_2$ is the end reaction force at bundle end 2 (Fig. 4(a)). An additional constraint on network evolution through process-A is that of mass conservation, i.e. $n\Sigma l_{ij} = const.$

Process-B, also referred to in this work as 'nodal relaxation', modifies $\{\delta_{ij}\}$. This changes the length of the nodal triangle sub-bundles and modifies $\{l_{ij}\}$ such to emulate the bundle zipping and unzipping processes. It is driven by the gradient of U_T in the phase space of $\{\delta_{ij}\}$. Referring to the geometry at a branching point shown Fig. 4(b), $\partial U_T/\partial \delta_{ij}$ is calculated as:

$$\frac{\partial U_T}{\partial \delta_{ij}} = -\frac{1}{2}\frac{n_1 n_2}{n_1 + n_2} E_f I_f \left\| \boldsymbol{\kappa}_1^+ - \boldsymbol{\kappa}_2^+ \right\|^2 + \gamma P(n_1 + n_2) - \gamma P(n_1) - \gamma P(n_2), \tag{2}$$

where, E_f is the elastic modulus of an individual fiber, n_1 and n_2 are the number of fibers in sub-bundles, $\boldsymbol{\kappa}_1^+$ and $\boldsymbol{\kappa}_2^+$ are the curvatures of the sub-bundles, and $\gamma P(n)$ is the adhesion energy of a bundle of n fibers. $P(n)$ is the number of line contacts between fibers in the bundle of n fibers. For close-packed bundles, $P(n) = 3n - \sqrt{12n-3}$ (Harborth, 1974). Eq. (2) was derived in Negi and Picu (2019b) and is only valid under the assumption that $I_b = nI_f$.

Evolution of the initial parametric model through the joint processes A and B leads to the desired stable structure, $\mathcal{S}$, of a nominal cellular network. To obtain the limit-case network from a given stable nominal cellular network, we increase the length of bundles from l_{ij} to l^*_{ij}, such that $\delta_{ij} = 0$. Further, we define MPC on the mesh nodes at bundle ends such to constrain the bundles to meet at 120°, as indicated for Case (2) in Fig. 2(a).

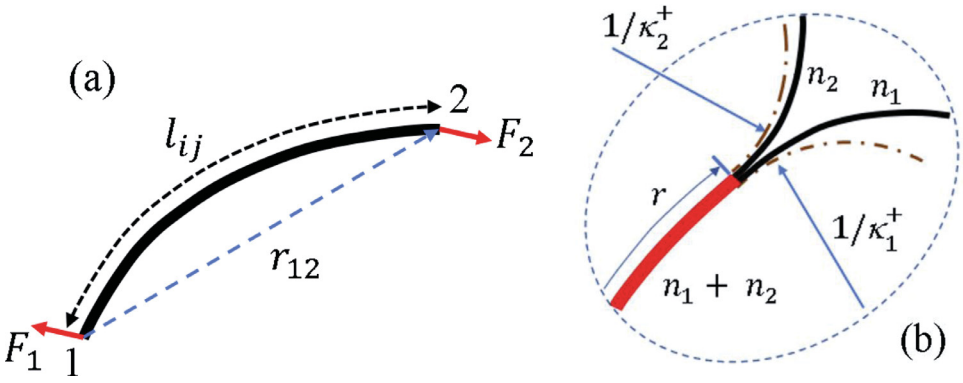

Fig. 4. (a) Representation of an individual bundle of $\mathcal{S}$. l_{ij} specifies the bundle length, $\boldsymbol{F_1}$ and $\boldsymbol{F_2}$ are the reaction forces acting at the two ends of the bundle. (b) Representation of bundle branching. r specifies the position of the branching point along the contour of a bundle and it is related to δ_{ij} parameter since $dr = -d\delta_{ij}$. n_1 and n_2 are sub-bundle sizes, and κ^+ are the sub-bundle curvatures at the branching point.

Periodic boundary conditions are applied as MPC on the mesh nodes at the in-plane boundaries. The model has dimensions λ_x and λ_y in the two directions of periodicity, which also make an angle θ_{xy}, Fig. 3. λ_x, λ_y, and θ_{xy} are additional degrees of freedom provided to the FE simulation and are not known a priori. λ_x, λ_y, and θ_{xy} thus refer to the macroscopic shape and size of a periodic cellular network and any applied macroscopic deformation on the network can be specified by modifying these parameters.

2.3. Solution procedure

Three realizations of each network are considered. These result from three Voronoi graphs. For each realization, we obtain stable nominal cellular networks by minimizing the total energy U_T through process-A and process-B acting simultaneously. To this end, a constrained gradient descent algorithm using the gradients of Eqs. (1) and (2) is performed and the network parameters, $\{l_{ij}, \delta_{ij}\}$, are evolved accordingly. Specifically, at each iteration the parametric model, $\mathcal{M}$, is used to setup the FE simulation which leads to the corresponding network structure, $\mathcal{S}$. The current structure is used to calculate the gradients of Eqs. (1) and (2), which allow evaluating the increments in the $\{l_{ij}, \delta_{ij}\}$ phase space, and to obtain the parameter set defining $\mathcal{M}$ of the next iteration. This procedure is similar to that used in Negi and Picu (2019b). The procedure continues until the minimum total energy is reached, while the total length of fiber bundles is maintained constant, periodicity is imposed on the global scale, and the overall graph topology is maintained. The limit case networks (Case (2)) are obtained from the nominal cellular networks by bringing parameters $\{\delta_{ij}\}$ to zero.

The number of fibers per bundle, n, is set to be 62 in all models. This implies that the bundle diameter is related to the fiber diameter as $d_b \sim 2.81 d_f$. The mean bundle length, l_C, for the limit-case (Case 2) network is equal to $160 d_f \sim 57 d_b$. The strength of adhesion is specified in terms of Ψ_d, which is a parameter of the problem. The fiber diameter d_f is taken as the unit of length and $E_f d_f^2$ is used as the unit of force.

Both Case (1) and Case (2), i.e. nominal cellular and limit-case networks, are loaded in uniaxial tension by modifying the model periodicity parameters, λ_x, λ_y and θ_{xy}. During the loading process, the minimum energy state is reached in each loading increment only through Process-B (zipping-unzipping of bundles).

3. Results and discussion

3.1. Structural characterization of cellular networks

A cellular network stabilized by adhesion differs from the graph-equivalent Voronoi network due to the presence of nodal triangles and prestress in the bundles. As discussed in Section 2, the prestress arises since the length distribution of bundles may not be entirely compatible with the angular constraints imposed by the nodal triangles.

The resulting structure is characterized by l_C and by the mean nodal triangle size $l_T = 2\overline{\delta_{ij}}$. l_T/l_C is a non-dimensional measure of the relative size of the nodal triangles and the connecting bundles. The prestress in bundles (outside triangles) can be characterized based on the respective bundle curvature. The root mean square curvature of the bundles in the network is denoted by K_{rms}, and the prestress is quantified by the non-dimensional product $l_C K_{rms}$, which describes the shape of the bundles.

We perform an image analysis of the structure in Fig. 1 obtained by explicitly simulating (using a bead spring model of the fibers) the self-organization process by which the network of bundles forms under the action of adhesion (Picu and Sengab, 2018) and infer that for this structure $l_T/l_C = 0.28$. We adjust the strength of adhesion, i.e. Ψ_d, to reach a value of this structural parameter close to the value evaluated for the structure in Fig. 1. Specifically, $\Psi_d = 23 \times 10^{-4}$ leads to $l_T/l_C = 0.23$. This value of Ψ_d is considered the reference value and is denoted by Ψ_0.

To study the effect of l_T/l_C on network properties, Ψ_d is varied from $\Psi_0/4$ to $2\Psi_0$ and the non-dimensional parameters l_T/l_C and $l_C K_{rms}$ are computed. In this parametric study, structures $\mathcal{S}$ with different Ψ_d are obtained from structure $\mathcal{S}_0$ (for which $\Psi_d = \Psi_0$) through process-B. The results are tabulated in Table 1 and also shown in Fig. 5. The variation of Ψ_d has a large effect on the network structure; the size of the nodal triangles, l_T, increases rapidly as Ψ_d decreases.

To provide a reference for this numerical result, we consider an analytic model of an isolated nodal triangle (Sengab and Picu, 2018), inset to Fig. 5. Consider, as above, that all bundles forming the node are composed from n fibers and the sub-bundles forming the triangle have $n/2$ fibers. The structure has three-fold symmetry, with all sub-bundles of given triangle having the same curvature. The geometry requires that

$$l_T = \pi R/3 \tag{3}$$

Table 1
Geometric properties of cellular networks with various levels of adhesion, Ψ_d. The values are the mean of three realizations.

Ψ_d	l_T/l_C	l_T/d_f	$l_C K_{rms}$
$2\Psi_0$	0.141	9.89	0.841
Ψ_0	0.230	14.93	0.624
$\Psi_0/2$	0.377	21.97	0.460
$\Psi_0/4$	0.651	31.53	0.339

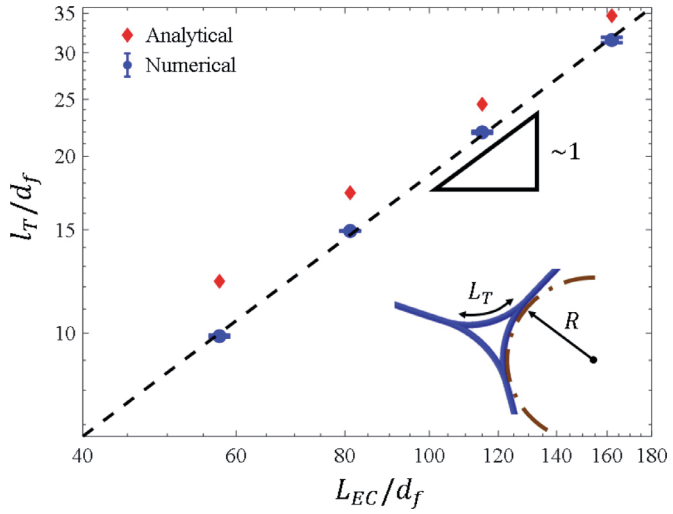

Fig. 5. Dependence of the mean nodal sub-bundle length, l_T, on the elastocapillary length, $L_{EC} = \sqrt{E_f I_f/\gamma} = d_f/\sqrt{\Psi_d}$. Both analytical (red diamonds), Eq. (5), as well as numerical (blue, solid circles) results are shown. The error bars show standard error from 3 realizations.

where R is the radius of curvature of the sub-bundles. R can be evaluated by imposing the condition of equilibrium of the branching points of a triangular structure:

$$R = \sqrt{\frac{nE_f I_f}{2(P(n) - 2P(n/2))\gamma}} \tag{4}$$

Hence, l_T/d_f can be expressed as:

$$\frac{l_T}{d_f} = \left(\frac{\pi}{3}\sqrt{\frac{n}{2(P(n) - 2P(n/2))}}\right)\frac{L_{EC}}{d_f} \tag{5}$$

where, $L_{EC} = \sqrt{E_f I_f/\gamma} = d_f/\sqrt{\Psi_d}$ .This relation is shown in Fig. 5 along with the numerical data.

In this analysis, Ψ_d is varied after the graph defining the network is defined. In this case, the variation of this parameter affects only the nodal triangle size and the residual stress in the structure, but not the overall graph. This somewhat artificial way of investigating the effect of adhesion is selected in view of the specific goal of the present study, i.e. that of determining the structural stability of the network once it is formed. In a broader sense, as discussed in Sengab and Picu (2018), Ψ_d controls the graph defining the network as well as the size of nodal triangles.

3.2. Mechanical behavior of cellular networks

The Cauchy stress vs. true strain response of nominal cellular networks with the reference set of parameters ($\bar{n} = 62$, $l_c^* = 160d$) and $l_T/l_C = 0.23$, 0.38, and 0.65 is shown in Fig. 6a. The stress is normalized with $\rho E_f A_f$, where ρ is the network density, A_f is the cross-sectional area of fibers, $A_f \sim d_f^2$, and the true strain, ε_t, is evaluated as the logarithm of the stretch, λ. The behavior is generally hyperelastic since no inelastic mechanism operates.

Fig. 6b shows the tangent stiffness $\hat{K} = \frac{1}{\rho E_f A_f}\frac{d\sigma}{d\varepsilon_t}$ versus the normalized stress, $\hat{\sigma} = \frac{\sigma}{\rho E_f A_f}$ computed based on the curves in Fig. 6a. Three regimes are visible: a linear elastic regime I (up to point A) in which $\hat{K}$ is constant, a first strain stiffening regime II in which the slope of the respective curve is $\beta = 1.4$ (A to B), and a second strain stiffening regime III in which a slope of ~0.5 develops (beyond B).

Two curves are shown for each value of l_T/l_C: one in which bundles may zip and unzip via Process-B, and a second curve obtained with geometrically identical networks in which nodal triangles are not allowed to evolve and retain the size at the beginning of loading. The second type of curve is shown with dashed line and is labeled "without Process-B". It is seen that the difference between the two curves is minimal. This indicates that, although the nodal triangles evolve during stretching, the contribution of this process to the overall stress-strain curve is minimal.

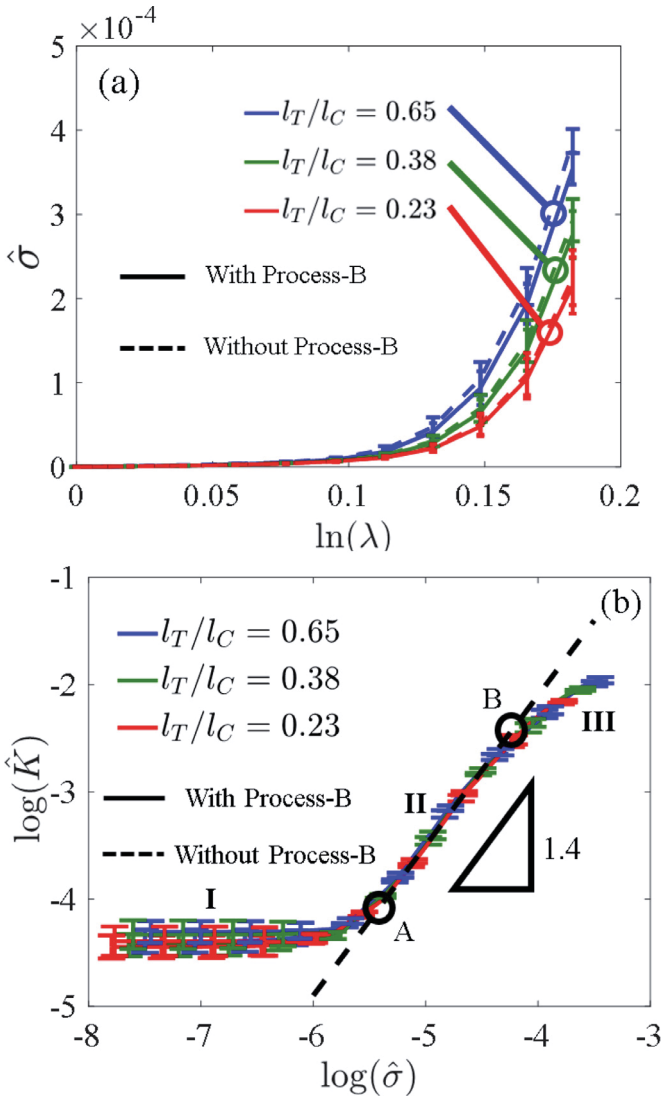

Fig. 6. (a) Stress-stretch curves for the uniaxial behavior of cellular networks with adhesion. The stress is normalized by $\rho E_f A_f$, $\hat{\sigma} = \frac{\sigma}{\rho E_f A_f}$. The continuous curves represent the response of the system in which nodal triangles evolve during loading, while the dashed lines represent networks in which triangles are prevented from evolving. (b) Data in (a) repotted as tangent stiffness vs. stress. The error bars show standard error from 3 realizations.

This is supported by Fig. 7a which shows the increase of the adhesion energy ΔU_γ and the strain energy ΔU_S during loading, for the network with $l_T/l_C = 0.65$. The variation of the strain energy in the structure is much more pronounced than the variation of the adhesion energy. Fig. 7b shows the variation of the mean triangle size, l_T, during deformation; it shows that nodal triangles deform and change size as the network is stretched. These results indicate that the network behaves as if it were crosslinked at the location of triangles. This is somewhat surprising, given the absence of physical crosslinks and indicates that nodal triangles are strongly stabilizing the structure.

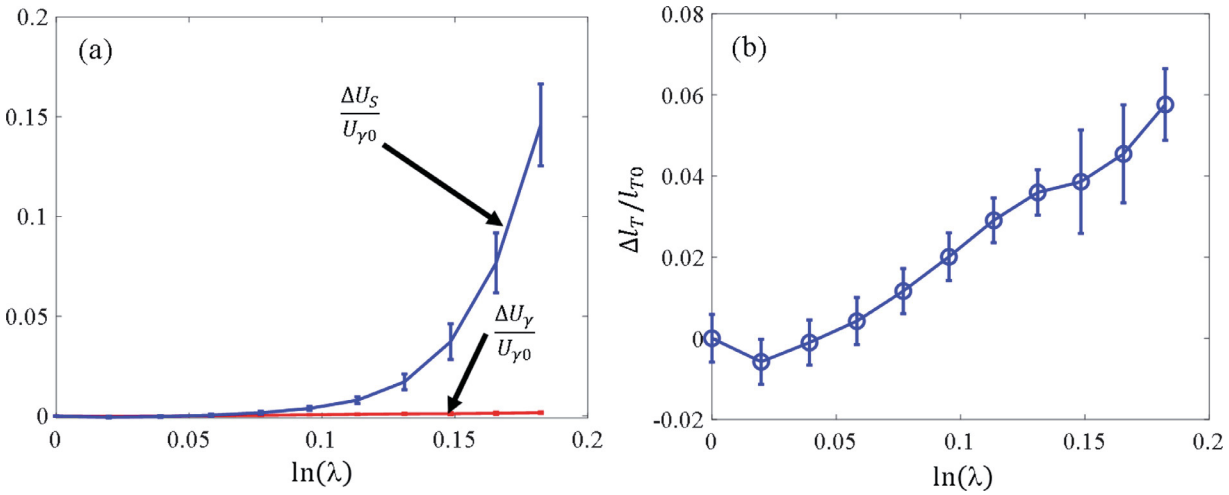

Fig. 7. (a) Variation of the adhesion, ΔU_γ, and strain energy ΔU_S, normalized by the adhesion energy of the unloaded network $U_{\gamma 0}$, during loading of nominal cellular network having $\Psi_d = \Psi_0/4$ and $l_T/l_C = 0.65$. (b) Variation of parameter l_T, Δl_T, defining the mean size of nodal triangles during loading. Δl_T is normalized with the value of l_T in the unloaded network, l_{T0}. The error bars show standard error from three realizations.

Further, we modify Ψ_d, which leads to a variation of l_T/l_C in the unloaded structures. Fig. 6b shows that this parameter has little effect on the stress-strain curves. The small strain stiffness changes little as Ψ_d is varied. Also, the nature of strain stiffening does not change. However, the stress-strain curves of Fig. 6a gradually shift to the right as l_T/l_C decreases, which indicates that only the transition strain between regimes I and II is affected, while the nature of strain stiffening is insensitive to this parameter. Specifically, as the strength of adhesion decreases, the range of the linear elastic regime I increases. A similar observation was made in Negi and Picu (2019b), where the mechanics of cross-linked networks with adhesion is discussed.

3.3. On the nature of strain stiffening

The nature of strain stiffening is defined by the slope of the regime II segment of the stiffness-stress curve in Fig. 6b. With $\hat{K} \sim \hat{\sigma}^\beta$ after a transition strain ε_0 (and stress σ_0, corresponding to point A in Fig. 6b), it results that the network strain stiffens as $\sigma/\sigma_0 = (1-(\beta-1)(\varepsilon/\varepsilon_0 - 1))^{-1/(\beta-1)}$ for $\varepsilon \geq \varepsilon_0$, in the strain stiffening regime II.

It is broadly reported in the literature that cross-linked networks of Voronoi type, whether in 2D or 3D, strain stiffen exponentially ($\beta = 1$) i.e. $\sigma/\sigma_0 = \exp(\varepsilon/\varepsilon_0 - 1)$ for $\varepsilon \geq \varepsilon_0$ (Ban et al., 2016; Deogekar and Picu, 2017; Licup et al., 2015). It was also reported that fibrous networks, i.e. networks created in 3D by the deposition of straight fibers with random positions and orientations, and crosslinked at all points of inter-fiber proximity, strain stiffen following a power law, with exponents β in the range [0.5,1) (Islam and Picu, 2018). Recent experimental results on reconstructed collagen networks also indicate the power-law strain stiffening behavior of the type $\hat{K} \sim \hat{\sigma}^\beta$, with β in the range 1 – 1.6 for temperature range 26–37 °C (Jansen et al., 2018).

It becomes of interest to investigate the origin of the strain stiffening observed here, with $\beta > 1$. To this end, we evaluate two hypotheses: (i) that the residual stress inherent in these cellular networks is at the origin of the modified strain stiffening behavior observed, and (ii) that this behavior is a consequence of the structure of the network and is not associated with adhesion or residual stress.

3.3.1. Effect residual stress

To evaluate the effect of the residual stress, we consider the nominal cellular network with nodal triangles characterized by $l_T/l_C = 0.23$. The residual stress in this structure is gradually increased by perturbing the length of the bundles as:

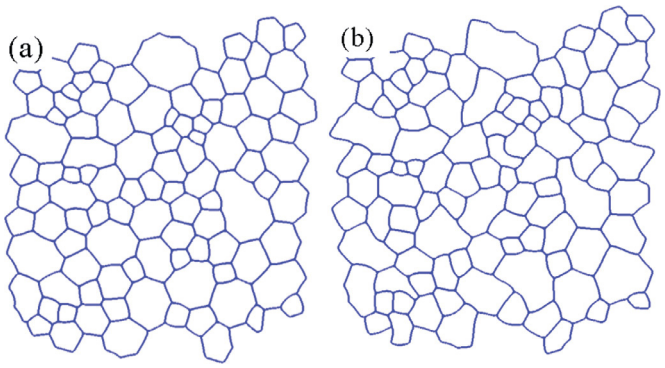

Fig. 8. A realization of the nominal cellular network structure, with $l_T/l_C = 0.23$, before (a) and after (b) bundle length perturbation with $c = 0.4$.

$$l'_{ij} = l_{ij}\left(1 + 2c\left(\xi_{ij} - 0.5\right)\right) \tag{6}$$

where l'_{ij} and l_{ij} are the lengths of a generic bundle after and before modification, respectively, ξ_{ij} is a stochastic variable uniformly distributed in the interval [0,1] and c is a parameter controlling the magnitude of the perturbation. Note that this structural modification disturbs the equilibrium between the adhesive forces and the force associated with the variation of the strain energy, and hence the perturbed model needs to be re-equilibrated after the bundle lengths are perturbed and before uniaxial testing. The nodal triangles are allowed to fully adjust during this equilibration to the new network configuration. Fig. 8a and b show a network before and after the bundle length modification and full relaxation. The curvature of bundles in Fig. 8b is larger, with the nondimensional parameter $l'_C K_b$ increasing from 0.62 for the structure in Fig. 8a, to 0.75 for the structure in Fig. 8b. As per Eq. (6), $\overline{l'}_T$ does not change upon perturbation. Interestingly, even after nodal relaxation, $\overline{l'}_T$, as well as the average size of the nodal triangles do not change. This is, in fact, an expected result based on the data in Fig. 5, which indicates that $\bar{\delta}$ depends only on the elastocapillarity length L_{EC}.

Fig. 9 shows the tangent stiffness-stress curve for the network with $c = 0$, and two perturbed cases, with $c = 0.2$ and 0.4. It is seen that the regime II slope remains $\beta = 1.4$ in networks with residual stress for all c values considered. This indicates that the origin of

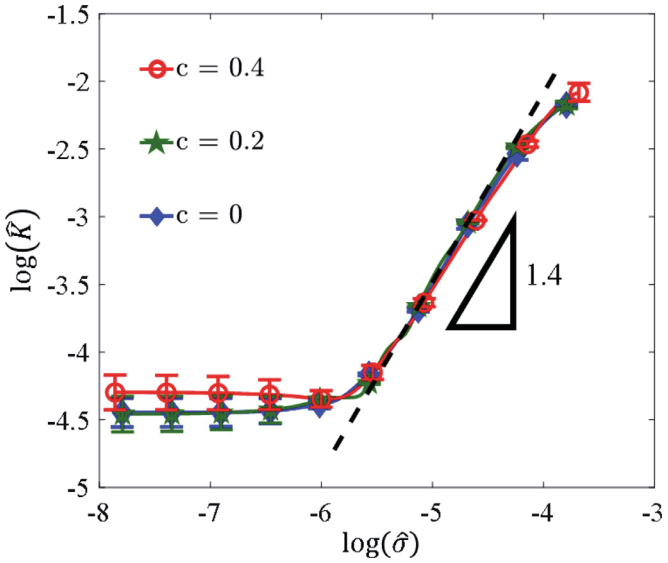

Fig. 9. Tangent stiffness $\hat{K}$ vs. stress $\hat{\sigma}$ curves for cellular networks with three levels of perturbation, c. The residual stress in the structure increases with c. Both stiffness and stress are normalized by $\rho E_f A_f$. The error bars show standard error for three realizations.

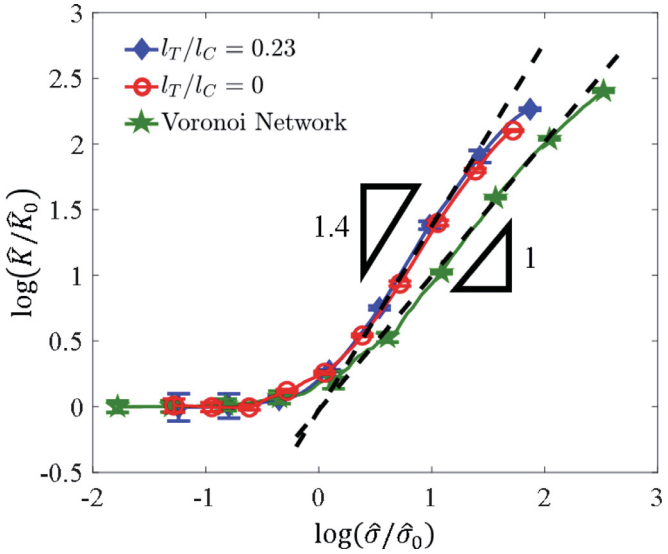

Fig. 10. Tangent stiffness vs. stress curves for $l_T/l_C = 0.23$ (blue diamonds) and $l_T/l_C = 0$ (red circles) and for a Voronoi network (green stars). Note that cellular networks with $l_T/l_C = 0.23$ undergo relaxation via the evolution of the nodal triangles during loading, which is not happening in the $l_T/l_C = 0$ case or the Voronoi network.

the modified strain stiffening behavior of cellular networks is not associated with the residual stress intrinsically present in these structures.

3.3.2. Effect of network architecture

The second hypothesis tested is that the functional form of strain stiffening is determined by the structure of the network. Fig. 10 shows the tangent stiffness-stress curve for the cellular network with $l_T/l_C = 0.23$ (Case (1)) and for the limit-case cellular network of Case (2), with $l_T/l_C \to 0$. In Case (2), the effect of adhesion is not present since triangles are eliminated. The two curves overlap, which demonstrates again that adhesion and the evolution of nodal triangles during network deformation do not contribute significantly to defining the stress-strain curve. Cellular networks with adhesion behave, in the range of strains considered and in the absence of relative fiber sliding within bundles, similar to crosslinked networks of the same graph. As discussed in Picu and Sengab (2018), this points to the strong stabilizing role of nodal triangles whose effective mechanical function results be to identical to that of a crosslink.

We include in Fig. 10 the tangent stiffness-stress curve for Voronoi networks. As expected, this curve exhibits in regime II a slope of 1 which implies exponential stiffening. It results that the nature of strain stiffening is controlled by the network architecture and not by the presence of residual stresses or the presence of adhesive interactions. This observation indicates that the functional form of the stress-stretch curve can be modified in a broad range by adjusting the underlying graph.

4. Conclusions

Previous work established that adhesive inter-fiber interactions drive the self-organization of ensembles of fibers. If adhesion is weak, self-organization does not take place and the fibers remain locked in the as-deposited mat configuration. If adhesion is sufficiently strong, cellular networks of fiber bundles result. Cellular networks are composed form fiber bundles which split and merge with other bundles at intersection points, forming characteristic nodal triangles. This preliminary work focused on the structure and stability of non-crosslinked fibrous assemblies stabilized by adhesion, but did not investigate their mechanics.

The present article discusses the mechanical behavior of cellular networks subjected to uniaxial tension. During loading triangles may evolve by zipping and unzipping, which leads to the variation of the length of adjacent bundles. Such networks of bundles store residual stresses and adhesion energy. The residual stress results from the incompatibility between the structure of the nodal triangles and the topological constraints of the network architecture. We observe that the stress-strain curve of networks in which triangles are allowed to evolve during loading, and that of the equivalent networks in which triangles are prevented from evolving, are approximately identical and have hyperelastic characteristics. Therefore, nodal triangles have a strong stabilizing effect causing the network to behave as if it were crosslinked. The stiffening behavior observed is different from that of the Voronoi networks. We show that this modified stiffening is due to the structure of the network, and not to the presence of residual stress or to inter-fiber adhesion. These results shed light on the behavior of buckypaper and of some collagen-based biological networks in which fiber bundles are observed.

Declaration of competing interest

The authors declare that they have no known competing financial interests or personal relationships that could have appeared to influence the work reported in this paper.

Acknowledgment

This work was supported by the NSF, US (US National Science Foundation) through grant No. CMMI-1634328.

Appendix A

The equilibrium configuration of an isolated nodal triangle is discussed in this Appendix. This was also analyzed in Picu and Sengab (2018); here we focus on the dependence of the inter-bundle angles on the variability of the structural parameters. To this end, consider the structure in Fig. A1, which shows a triangle formed by three bundles, AA', BB', and CC' of n_1, n_2 and n_3 fibers, respectively. The outer ends of the bundles are free. This represents an isolated nodal triangle or a nodal triangle in a network in which bundles

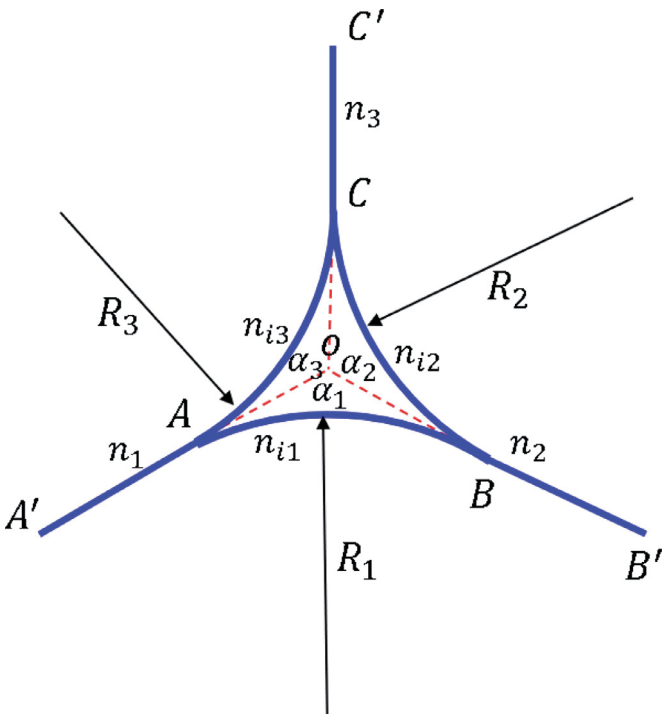

Fig. A1. Parameters defining a nodal triangle.

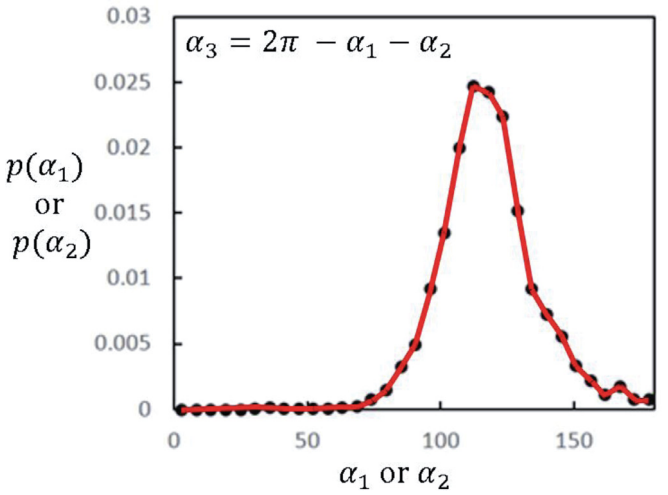

Fig. A2. Probability distribution function of angles α_1 and α_2 defining the geometry of a minimum energy triangle with variable bundle sizes, n_1, n_2 and n_3. Triangles with very different values of n_i take almost symmetric configurations with α_1, α_2 and α_3 close to 120°.

remain straight and store no strain energy. The sub-bundles AB, AC and BC store strain energy and are arcs of circle of radii R_1, R_2 and R_3. At the splitting points A, B and C, the sub-bundles are tangent to each other. Bundles AA', BB' and CC' form angles α_1, α_2 and α_3.

The total energy of this structure, U_T, including strain and adhesion energy components, can be calculated in terms of these parameters. For each set n_i, $i=1\ldots3$, minimization of the total energy provides the equilibrium angles α_i, $i=1\ldots3$ (restricted by the condition $\alpha_1+\alpha_2+\alpha_3=2\pi$). This procedure is applied to a large number of configurations with bundle sizes n_1, n_2 and n_3 sampled from a discrete, binomial distribution of set mean and broad and adjustable variance. Fig. A2 shows the probability distribution function of angles α_1 and α_2. Although the distribution of n_i is broad, the triangle configuration that minimizes the total energy is close to being equilateral, with $\alpha_1=\alpha_2=\alpha_3\approx 120°$.

Appendix B

In this Appendix, we derive the approximation of the gradient of the total network energy U_T with respect to the variation of one of the bundle lengths, l_{ij}, used in the minimization procedure, Eq. (1). For simplicity of notations, we drop the indices ij in this appendix.

Consider a fiber of length l in a network as shown in Fig. B1(a). Let U be the total strain energy of the network and u be the strain energy of this particular fiber. Let $\mathbf{r}$ be the position vector of node B from node A and $\mathbf{F}$ be the end reaction force acting on the fiber at node B. Three steps are taken to find $\partial U/\partial l$:

Step 1: decouple the fiber from the network at the nodes and fix the kinematic boundary conditions at the nodes for both the fiber and the reminder of the network.

The fiber is then scaled by a factor α, where $\alpha=1+d\alpha$ and $d\alpha=dl/l$, as shown in Fig. B1(b). The increment in the energy of the fiber du is:

$$du=\left(\frac{\partial u}{\partial \alpha}\right)_{\alpha=1} d\alpha \tag{B.1}$$

The end reaction force $\mathbf{F}$ change by $d\mathbf{F}$ such that $d\mathbf{F}=\mathbf{h}d\alpha$, where $\mathbf{h}$ is the gradient of $\mathbf{F}$ with respect to α. The relative position of the fiber nodes, $\mathbf{r}$, changes by $d\mathbf{r}$ and $d\mathbf{r}=\mathbf{r}d\alpha$ for affine scaling. Note that the affine scaling does not change the tangent versors at the end nodes.

Step 2: the fiber is deformed and re-coupled with the surrounding network, fulfilling the original kinematic boundary conditions, as shown in Fig. B1(c). At the end of this operation, the forces at the end nodes are again modified and can be generically shown as $\mathbf{F}+\mathbf{g}d\alpha$, where $\mathbf{g}$ is an unknown gradient vector. The net work done on the fiber to re-establish the original kinematic boundary conditions is dw and reads:

$$dw=-(\mathbf{F}+0.5(\mathbf{g}+\mathbf{h})d\alpha)\cdot d\mathbf{r} \tag{B.2}$$

In principle, the moments at the end nodes, $\mathbf{M}$, may also need to be modified to satisfy the kinematic boundary conditions in this step. However, since the tangent versors remain unchanged in the process, the moments do not contribute to the work increment, dw.

Replacing $d\mathbf{r}=\mathbf{r}d\alpha$ and ignoring higher order terms in Eq. (B.2), we obtain

$$dw=-\mathbf{F}\cdot\mathbf{r}d\alpha \tag{B.3}$$

Therefore, the net strain energy increment with respect to the initial configuration at the end of Step 2, du', is

$$du'=\left(\left(\frac{\partial u}{\partial \alpha}\right)_{\alpha=1}-\mathbf{F}\cdot\mathbf{r}\right)d\alpha \tag{B.4}$$

Step 3: release the kinematic boundary conditions at the end nodes of the fiber and allow the system to re-equilibrate, as shown in Fig. B1(d). Let the difference in the energy of the fiber in the final configuration, Fig. B1(d), and the initial configuration, Fig. B1(a), be du'':

$$du''=du'+du_{rd} \tag{B.5}$$

where, du_{rd} is the energy variation in the fiber due to the redistribution between itself and the surrounding network.

Likewise, the incremental change in the energy of the surroundings, i.e. the network excluding the fiber, is dU_{rd}^{surr}. Therefore, the increment of total energy of the network dU can be written:

$$dU=\left(\left(\frac{\partial u}{\partial \alpha}\right)_{\alpha=1}-\mathbf{F}\cdot\mathbf{r}\right)d\alpha+du_{rd}+dU_{rd}^{surr} \tag{B.6}$$

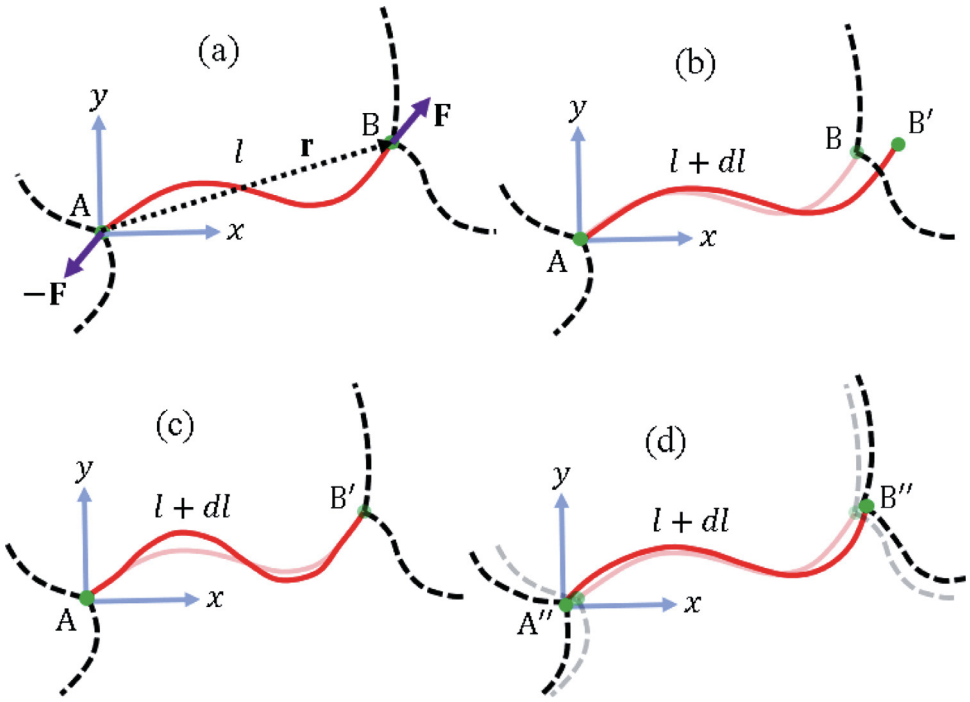

Fig. B1. Process used to evaluate the approximation of the network energy gradient of Eq. (1). (a) Initial configuration of a fiber of length l in a network. $\mathbf{r}$ is the position vector of node B relative to node A and $\mathbf{F}$ is the reaction force acting on the fiber at B (b) Affine scaling of the fiber (with node A as center) by $(1+dl/l)$ (c) Reapplying the initial kinematic boundary conditions to the scaled fiber (d) Relaxing the nodes for re-equilibration of the system.

where, du_{rd} and dU_{rd}^{surr} are unknown energy increments of order $O(d\alpha)$. However, since the final configuration, Fig. B1(d), is at equilibrium and the configuration of Fig. B1(c) is infinitesimally close to it (by order $O(d\alpha)$), the strain energy exchange between the fiber and its surrounding, i.e. $du_{rd} + dU_{rd}^{surr}$, must be of order $O(d\alpha^2)$. Therefore, Eq. (B.6) reduces to:

$$dU = \left(\left(\frac{\partial u}{\partial \alpha}\right)_{\alpha=1} - \mathbf{F}\cdot\mathbf{r}\right)d\alpha + O\left(d\alpha^2\right) \tag{B.7}$$

Ignoring the higher order terms in Eq. (B.7) it results:

$$\frac{\partial U}{\partial \alpha} = \left(\left(\frac{\partial u}{\partial \alpha}\right)_{\alpha=1} - \mathbf{F}\cdot\mathbf{r}\right) \tag{B.8}$$

For any curved fiber in equilibrium, u, has bending energy (u_{BE}), axial energy (u_{AE}), and shear energy (u_{SE}) components. The affine deformation of the fiber by factor α in Step 1 leads to the variation of these quantities as:

$$u_{BE}(\alpha) = \frac{u_{BE}}{\alpha},\ u_{AE}(\alpha) = \frac{u_{AE}}{\alpha^3},\ u_{SE}(\alpha) = \frac{u_{SE}}{\alpha^3} \tag{B.9}$$

Eq. (B.9) results by solving the static equilibrium equation of a fiber whose curvature is not trivially zero throughout.

Therefore, $(\frac{\partial u}{\partial \alpha})_{\alpha=1}$ in Eq. (B.8) can be written:

$$\left(\frac{\partial u}{\partial \alpha}\right)_{\alpha=1} = -(u_{BE} + 3u_{AE} + 3\ u_{SE}) \tag{B.10}$$

and considering $d\alpha = dl/l$ it results:

$$\frac{\partial U}{\partial l} = -\ \frac{(u_{BE} + 3u_{AE} + 3\ u_{SE} + \mathbf{F}\cdot\mathbf{r})}{l} \tag{B.11}$$

References

Alava, M., Niskanen, K., 2006. The physics of paper. Rep. Prog. Phys. doi:10.1088/0034-4885/69/3/R03.

Ban, E., Barocas, V.H., Shephard, M.S., Picu, R.C., 2016. Softening in random networks of non-identical beams. J. Mech. Phys. Solids 87, 38–50. doi:10.1016/j.jmps.2015.11.001.

Berhan, L., Yi, Y.B., Sastry, A.M., Munoz, E., Selvidge, M., Baughman, R., 2004. Mechanical properties of nanotube sheets: alterations in joint morphology and achievable moduli in manufacturable materials. J. Appl. Phys. 95, 4335–4345. doi:10.1063/1.1687995.

Bico, J., Roman, B., Moulin, L., Boudaoud, A., 2004. Elastocapillary coalescence in wet hair. Nature 432, 690. doi:10.1038/432690a.

Carpick, R.W., Agraït, N., Ogletree, D.F., Salmeron, M., 1996. Variation of the interfacial shear strength and adhesion of a nanometer-sized contact. Langmuir 12, 3334–3340. doi:10.1021/la9509007.

Coleman, J.N., Blau, W.J., Dalton, A.B., Muñoz, E., Collins, S., Kim, B.G., Razal, J., Selvidge, M., Vieiro, G., Baughman, R.H., 2003. Improving the mechanical properties of single-walled carbon nanotube sheets by intercalation of polymeric adhesives. Appl. Phys. Lett. 82, 1682–1684. doi:10.1063/1.1559421.

De Volder, M., Hart, A.J., 2013. Engineering hierarchical nanostructures by elastocapillary self-assembly. Angew. Chem. 52, 2412–2425. doi:10.1002/anie.201205944.

Deogekar, S., Picu, R.C., 2017. Structure-properties relation for random networks of fibers with noncircular cross section. Phys. Rev. E 95, 1–5. doi:10.1103/PhysRevE.95.033001.

Ducrot, E., Chen, Y., Bulters, M., Sijbesma, R.P., Creton, C., 2014. Toughening elastomers with sacrificial bonds and watching them break. Science 80 (344), 186–189. doi:10.1126/science.1248494.

Gong, J.P., 2014. Materials both tough and soft. Science 80 (344), 161–162. doi:10.1126/science.1252389.

Harborth, H., 1974. Solution to problem 664. Elem. Math. 29, 14.

Homola, A.M., Israelachvili, J.N., McGuiggan, P.M., Gee, M.L., 1990. Fundamental experimental studies in tribology: the transition from "interfacial" friction of undamaged molecularly smooth surfaces to "normal" friction with wear. Wear 136, 65–83. doi:10.1016/0043-1648(90)90072-I.

Islam, M.R., Picu, R.C., 2018. Effect of network architecture on the mechanical behavior of random fiber networks. J. Appl. Mech. 85, 081011. doi:10.1115/1.4040245.

Jansen, K.A., Licup, A.J., Sharma, A., Rens, R., MacKintosh, F.C., Koenderink, G.H., 2018. The role of network architecture in collagen mechanics. Biophys. J. 114, 2665–2678. doi:10.1016/j.bpj.2018.04.043.

Licup, A.J., Münster, S., Sharma, A., Sheinman, M., Jawerth, L.M., Fabry, B., Weitz, D.A., MacKintosh, F.C., 2015. Stress controls the mechanics of collagen networks. Proc. Natl. Acad. Sci. U. S. A. doi:10.1073/pnas.1504258112.

Liu, J., Rinzler, A.G., Dai, H., Hafner, J.H., Kelley Bradley, R., Boul, P.J., Lu, A., Iverson, T., Shelimov, K., Huffman, C.B., Rodriguez-Macias, F., Shon, Y.S., Lee, T.R., Colbert, D.T., Smalley, R.E., 1998. Fullerene pipes. Science 80 (280), 1253–1256. doi:10.1126/science.280.5367.1253.

Lu, J.P., 1997. Elastic properties of carbon nanotubes and nanoropes. Phys. Rev. Lett. 79, 1297–1300. doi:10.1103/PhysRevLett.79.1297.

Michielsen, S., Pourdeyhimi, B., Desai, P., 2006. Review of thermally point-bonded nonwovens: materials, processes, and properties. J. Appl. Polym. Sci. 99, 2489–2496. doi:10.1002/app.22858.

Negi, V., Picu, R.C., 2019a. Mechanical behavior of nonwoven non-crosslinked fibrous mats with adhesion and friction. Soft Matter 15, 5951–5964. doi:10.1039/c9sm00658c.

Negi, V., Picu, R.C., 2019b. Mechanical behavior of cross-linked random fiber networks with inter-fiber adhesion. J. Mech. Phys. Solids 122, 418–434. doi:10.1016/j.jmps.2018.09.027.

Picu, R.C., Sengab, A., 2018. Structural evolution and stability of non-crosslinked fiber networks with inter-fiber adhesion. Soft Matter 14, 2254–2266. doi:10.1039/c7sm02555f.

Rens, R., Vahabi, M., Licup, A.J., MacKintosh, F.C., Sharma, A., 2016. Nonlinear mechanics of athermal branched biopolymer networks. J. Phys. Chem. B 120, 5831–5841. doi:10.1021/acs.jpcb.6b00259.

Schofield, J., 1938. 21—Researches on wool felting. J. Text. Inst. Trans. 29, T239–T252. doi:10.1080/19447023808658850.

Sengab, A., Picu, R.C., 2018. Filamentary structures that self-organize due to adhesion. Phys. Rev. E 97, 032506. doi:10.1103/PhysRevE.97.032506.

Stallard, J.C., Tan, W., Smail, F.R., Gspann, T.S., Boies, A.M., Fleck, N.A., 2018. The mechanical and electrical properties of direct-spun carbon nanotube mats. Extrem. Mech. Lett. 21, 65–75. doi:10.1016/j.eml.2018.03.003.

Style, R.W., Jagota, A., Hui, C.-Y., Dufresne, E.R., 2017. Elastocapillarity: surface tension and the mechanics of soft solids. Annu. Rev. Condens. Matter Phys. 8, 99–118. doi:10.1146/annurev-conmatphys-031016-025326.

Subramanian, G., Picu, C.R., 2011. Mechanics of three-dimensional, nonbonded random fiber networks. Phys. Rev. E 83, 056120. doi:10.1103/PhysRevE.83.056120.

Tempel, M., Isenberg, G., Sackmann, E., 1996. Temperature-induced sol-gel transition and microgel formation in α-actinin cross-linked actin networks: a rheological study. Phys. Rev. E 54, 1802–1810. doi:10.1103/PhysRevE.54.1802.

Toll, S., Manson, J.-A.E., 1995. Elastic compression of a fiber network. J. Appl. Mech. 62, 223. doi:10.1115/1.2895906.

van Wyk, C.M., 1946. Note on the compressibility of wool. J. Text. Inst. Trans. 37, T285–T292. doi:10.1080/19447024608659279.

Yunoki, S., Hatayama, H., Ebisawa, M., Kondo, E., Yasuda, K., 2015. A novel fabrication method to create a thick collagen bundle composed of uniaxially aligned fibrils: an essential technology for the development of artificial tendon/ligament matrices. J. Biomed. Mater. Res. 103, 3054–3065. doi:10.1002/jbm.a.35440.

Zilman, A.G., Safran, S.A., 2003. Role of cross-links in bundle formation, phase separation and gelation of long filaments. Europhys. Lett. 63, 139–145. doi:10.1209/epl/i2003-00489-5.